

## Effects of heartbeat and respiration on macaque fMRI: Implications for functional connectivity

Tobias Teichert<sup>a,\*</sup>, Jack Grinband<sup>a,b</sup>, Joy Hirsch<sup>b</sup>, Vincent P. Ferrera<sup>a</sup>

<sup>a</sup> Columbia University, Department of Psychiatry and Neuroscience, David Mahoney Centre for Brain and Behavior Research, New York, USA

<sup>b</sup> Columbia University, Neurological Institute, Program for Imaging & Cognitive Sciences (PICCS), New York, USA

### ARTICLE INFO

#### Article history:

Received 3 July 2009

Received in revised form 26 October 2009

Accepted 27 November 2009

Available online 5 December 2009

#### Keywords:

fcMRI

Macaque

Functional connectivity

Resting state

### ABSTRACT

The use of functional magnetic resonance imaging (fMRI) in non-human primates is on the increase. It is known that the blood-oxygen-level-dependent (BOLD) signal varies not only as a function of local neuronal energy consumption but also as a function of cardiac and respiratory activity. We mapped these cyclic cardiac and respiratory artifacts in anesthetized macaque monkeys and present an objective analysis of their impact on estimates of functional connectivity (fcMRI). Voxels with significant cardiac and respiratory artifacts were found in much the same regions as previously reported for awake humans. We show two example seeds where removing the artifacts clearly decreased the number of false positive and false negative correlations. In particular, removing the artifacts reduced correlations in the so-called resting state network. Temporal bandpass filtering or spatial smoothing may help to reduce the effects of artifacts in some cases but are not an adequate replacement for an algorithm that explicitly models and removes cyclic cardiac and respiratory artifacts.

© 2009 Elsevier Ltd. All rights reserved.

### 1. Introduction

Recent years have seen an increase in the number of fMRI studies using anesthetized as well as awake macaque monkeys (e.g., Brewer, Press, Logothetis, & Wandell, 2002; Essen et al., 2001; Hadj-Bouziane, Bell, Knutsen, Ungerleider, & Tootell, 2008; Logothetis, Guggenberger, Peled, & Pauls, 1999; Pinsk, DeSimone, Moore, Gross, & Kastner, 2005; Tsao, Freiwald, Knutsen, Mandeville, & Tootell, 2003; Vincent et al., 2007). Such studies provide a unique opportunity to bridge the gap between invasive single cell electrophysiology in monkeys and non-invasive fMRI methods in humans. Vincent et al. (2007) were recently able to show that measures of functional connectivity yield meaningful results even in anesthetized monkeys. This finding amplifies the potential range of applications of monkey imaging.

The BOLD signal is modulated by several physiological artifacts such as fluctuations in breathing rate and amplitude as well as pulsatile and respiratory motion. It is still a matter of debate to what extent measures of functional connectivity represent such artificial processes (for reviews see Auer, 2008; Rogers, Morgan, Newton, & Gore, 2007). The current study focuses exclusively on blood volume, blood oxygenation, and motion artifacts with a fixed phase

relation to the cardiac and respiratory cycle. These artifacts will be referred to as cyclic physiological artifacts or simply cyclic artifacts. Cyclic artifacts have long been known to affect human BOLD signals (e.g., Biswal, DeYoe, & Hyde, 1996; Dagli, Ingeholm, & Haxby, 1999; Glover, & Lee, 1995; Glover, Li, & Ress, 2000; Harvey et al., 2008; Hu, Le, Parrish, & Erhard, 1995; Lowe, Mock, & Sorenson, 1998; Lund, 2001a; Lund, Madsen, Sidaros, Luo, & Nichols, 2006; Mitra, Ogawa, Hu, & Ugurbil, 1997; Raj, Anderson, & Gore, 2001). Despite the current interest in monkey fMRI, cyclic artifacts of this species have not been quantified.

The detection and removal of cyclic artifacts may be of great importance for fcMRI, especially when using long TRs (Auer, 2008; Cordes et al., 2001; Lowe et al., 1998; Lund, 2001a; Maldjian, 2001; Mitra et al., 1997; Rogers et al., 2007). Lund (2001a) has argued that with long TRs cyclic artifacts may be aliased into lower frequency bands which are typically used for fcMRI. Further, Lowe et al. (1998) have shown that the spatial specificity of fcMRI is reduced when using long TRs, the most likely cause being aliased cyclic artifacts. However, despite the potential impact of cyclic artifacts on fcMRI and the availability of tools to remove them (e.g., RETROICOR, Glover et al., 2000), a large number of studies do not make use of this possibility (for a review of clinical studies see Auer, 2008).

One reason for this might be that so far, no study has actually compared standard whole-brain connectivity maps before and after removal of cyclic artifacts. Previous studies which have analyzed cyclic artifacts (e.g., Glover et al., 2000; Harvey et al., 2008; Lund et al., 2006), only show maps of the affected regions (susceptibility maps). However, the fact that two voxels are both affected

\* Corresponding author at: Columbia University, Neuroscience, 40 Haven Ave, New York, NY 10032, USA. Tel.: +1 212 543 6931x305.

E-mail addresses: [tt2288@columbia.edu](mailto:tt2288@columbia.edu) (T. Teichert), [jg2269@columbia.edu](mailto:jg2269@columbia.edu) (J. Grinband), [jh2155@columbia.edu](mailto:jh2155@columbia.edu) (J. Hirsch), [vpf3@columbia.edu](mailto:vpf3@columbia.edu) (V.P. Ferrera).

by cardiac artifacts, does not automatically imply that they will have correlated artifacts. For example, if the artifact  $a_1$  follows the sine of the cardiac cycle in one voxel,  $a_1 = \sin(\phi)$ , and the cosine of the cardiac cycle in another region,  $a_2 = \cos(\phi)$ , they are effectively uncorrelated. Also, it is important to consider differences in slice-time acquisition which will cause different voxels to be sampled at different phases of the cardiac and respiratory cycle. Depending on the average phase shift introduced by the difference in slice-timing, two voxels with identical dependence on cardiac and respiratory activity may show significant positive, negative or no correlation.

Further, standard fcMRI preprocessing steps typically involve explicit as well as implicit spatial low-pass filtering. Artifacts in adjacent slices are not necessarily sampled in a similar phase of the artifact, thus introducing high spatial frequencies perpendicular to the slice orientation. Thus, spatial smoothing may reduce the amplitude of the cyclic artifacts to a larger degree than other signals. In summary, the relation between susceptibility maps on the one hand, and fcMRI maps on the other is not immediately obvious and merits empirical investigation.

The present study has two primary goals. First, it provides a quantitative assessment of cyclic artifacts in macaque monkeys, analogous to previous studies in humans (Cordes et al., 2001; Glover et al., 2000; Harvey et al., 2008; Lund et al., 2006). Second, it analyses the effects of removing cyclic artifacts on standard whole-brain functional connectivity maps of anesthetized macaques. We find that, indeed, cyclic artifacts quantitatively affect estimates of functional connectivity and may lessen our ability to detect and quantify functional networks.

## 2. Materials and methods

### 2.1. Imaging

Three adult male macaque monkeys (macaca mulatta, 7–10 kg) were scanned under light isoflurane anesthesia (0.8–1.1%, spontaneous ventilation) on a 3T Philips scanner. The monkeys were scanned in the supine position while head motion was restrained by padding placed between the head and the headcoil. In the initial phase of the anesthesia, resting state T2\*-weighted functional images were acquired (TR=2000 ms, TE=25 ms, flip-angle=72°, FOV: 192 mm × 160 mm × 50 mm, 96 × 96 × 25 2 mm<sup>3</sup> isotropic voxels, 400 volumes per series). Slices were acquired with the standard Philips ventral to dorsal interleaved sequence. Subsequently, under deeper anesthesia, T1-weighted structural images were taken (256 × 256 × 100 1 mm<sup>3</sup> isotropic voxels).

### 2.2. Physiological measures

During functional scans, cardiac activity was derived from peripheral blood oxygenation measured with a pulse-oximeter placed on one of the monkey's toes. The spontaneous respiratory activity was monitored by measuring end-tidal CO<sub>2</sub>-concentration. These signals, i.e., the cardiac signal  $C(t)$  and the respiratory signal  $R(t)$  were sampled and digitized at a rate of 200 Hz and saved alongside the slice triggers from the scanner.

Following Hu et al. (1995) and Glover et al. (2000) we defined the phase of the cardiac signal  $\phi_C$  by the following equation:

$$\phi_C(t) = \frac{2\pi(t - t_{pre})}{t_{post} - t_{pre}}$$

Here  $t_{pre}$  and  $t_{post}$  are the two local maxima in peripheral blood oxygenation preceding and following  $t$ . Hence,  $\phi_C$  advances at a steady pace within each cardiac cycle. The rate of change of  $\phi_C$  differs between cycles of different duration. In contrast to Glover et al. (2000) we used the same method to derive an estimate of phase of the respiratory cycle,  $\phi_R$  (see Section 2.3 for details).

To detect the local maxima of  $C(t)$  and  $R(t)$ , we first filtered out high frequencies using Gaussian kernels with a standard deviation of 25 and 200 ms for  $C$  and  $R$ , respectively. Subsequently, we calculated time derivatives of the signals by subtracting a lagged version of the same signal:

$$\frac{dx}{dt}[n] = \nu \delta_t (\times [n] - x[t - \nu])$$

Here  $\delta$  corresponds to the temporal resolution, in our case 1/200 and  $\nu$  to the lag which was chosen as 1 and 2 for  $C$  and  $R$ , respectively. Local maxima were detected when the sign of the derivative switched from positive to negative.

### 2.3. Artifact removal

In the present study we used harmonic or trigonometric regression (e.g., Mardia, 1972) to detect and remove cyclic cardiac and respiratory artifacts. Briefly, the method assumes that the raw BOLD signal is the result of neuronally driven changes in BOLD and artificial changes in BOLD related to cardiac and respiratory activity, respectively:

$$B_{raw}(t) = B_N(t) + B_C(t) + B_R(t)$$

Further, it is assumed that both  $B_C$  and  $B_R$  are functions of the phase of the cardiac and respiratory cycle, respectively:

$$B_C(t) = a_C[\phi_C(t)]$$

$$B_R(t) = a_R[\phi_R(t)]$$

Here  $a_C$  and  $a_R$  describe the effect of an average cardiac or respiratory cycle on BOLD as a function of phase. In order to visualize  $a_C$  and  $a_R$  we plot the raw BOLD activity  $B_{raw}$  not as a function of time, but as function of the current phase  $\phi_C(t)$  and  $\phi_R(t)$ , respectively (see supplementary Figs. S1b&c and S2b&c, respectively). The functions  $a_C$  and  $a_R$  can be estimated in several ways. In the present paper we used harmonic regression to fit a subset of orthogonal basis functions to the data. The functions we fit consist of a constant offset plus the first  $N$  Fourier components:

$$a_{C/R}[\phi] = \alpha_0 + \sum_{\omega=1}^N \alpha_{\omega} \sin[\omega\phi_{C/R}] + \beta_{\omega} \cos[\omega\phi_{C/R}]$$

Thus, for each of the two artifacts the entire model is determined by  $1 + 2N$  parameters. In the present paper we used  $N = 6$ , unless stated otherwise. To remove the artifact we subtracted the estimated artifact from the raw data.

$$B_{clean}(t) = B_{raw}(t) - a_C[\phi_C(t)] - a_R[\phi_R(t)]$$

The standard harmonic regression which we used here is highly similar to the RETROICOR method described by Glover et al. (2000). RETROICOR differs from standard harmonic regression in its treatment of the respiratory artifacts. The respiratory artifact is thought to arise from apparent motion caused by changes in bulk susceptibility in the lungs (Raj et al., 2001). Hence, the artifact is supposed to depend not only on the phase of the respiratory cycle, but also on the amplitude. RETROICOR treats this dependency by introducing a different estimate of phase (see Glover et al., 2000 for details). We decided not to use this alternative estimate of phase for two reasons. First, we observed very little variability in the amplitude of the respiratory cycles. Thus, our method and RETROICOR, produce virtually identical estimates of phase with correlation coefficients on the order of .975. Second, if amplitudes do vary, the RETROICOR phase estimate will have discontinuities in phase space (Supplementary Fig. 3, top panel). This will cause the sine-regressors to have discontinuities in the time domain (Supplementary Fig. 3, bottom panel) which do not match the continuous nature of the respiratory artifact.

It is important to note that harmonic regression does not assume constant frequency of the cardiac and respiratory signals. However, it does implicitly assume that the functions  $a_C$  and  $a_R$  are constant over the time and frequency range of the cardiac and respiratory signals during data acquisition. Deviations from this assumption will cause the model to underestimate the amount of variance caused by cardiac and respiratory artifacts.

We used standard statistical methods to describe the model fit.  $F$ -values were calculated as the fraction of the sums of squares of the model  $SSQ_{mod}$  and the sums of squares of the residuals  $SSQ_{res}$  normalized with the respective degrees of freedom,  $F = (SSQ_{mod}/df_{mod})/(df_{res}/SSQ_{res})$ . The model was considered to provide a significant fit to the data if the  $F$ -value exceeded the 0.95-quantile of an  $F$  distribution with the corresponding degrees of freedom. The percent variance explained (%Var) was calculated as 1 minus the fraction of the sums of squares of the residuals and the sums of squares of the original data, %Var =  $1 - (SSQ_{res}/SSQ_{raw})$ . For fixed degrees of freedom (as was the case here) there is a simple relation between the  $F$ -values and the percent variance explained: the percent variance explained corresponds to the fraction of the  $F$ -value and the sum of the  $F$ -value and the fraction of the degrees of freedom, %Var =  $F/(F + (df_{res}/df_{mod}))$ . In the current case, with  $13 - 1 = 12$  numerator and  $394 - 12 - 1 = 381$  denominator degrees of freedom the critical  $F$ -value (see above) corresponds to 1.78. This  $F$ -value, in turn, corresponds to 5.3% variance explained.

### 2.4. Preprocessing

For all runs we used two different preprocessing protocols, one of which used the harmonic regression method. The leading six volumes were removed to avoid onset non-stationarities. A functional reference volume was drawn halfway through the scan ( $(400 - 6)/2 = 197$ ). All the voxels with intensity values in the lower 5-percentile in any of the 394 volumes were masked out.

The following steps were executed only if the harmonic regression method was applied. Using FSL's math routine (*fslmaths*, Smith et al., 2004) the shortened and masked series was highpass-filtered with a cutoff wavelength of 400 s. From the

highpassed data we estimated and removed cardiac and respiratory artifacts with the phase-regression method described above. The removed artifacts were stored for further analysis. The previously removed low frequency components were added to the artifact-free data to make the two data sets with and without the artifacts identical in every other aspect.

From here on the two preprocessing pipelines were identical. FSL's motion correction algorithm (*mcflirt*, Jenkinson, Bannister, Brady, & Smith, 2002) was used to register all volumes to the reference functional volume. Typically, the motion was small, well below the dimensions of a single voxel ( $2\text{ mm}^3$ ). FSL's slice-time-correction algorithm (*slicetimer*, Smith et al., 2004) was used to correct for differences of slice-time acquisition between different slices of a volume. Finally, using FSL's linear registration tool (*flirt*, Jenkinson et al., 2002) this data set was registered to a global reference volume which corresponded to the first high-contrast functional volume of the fourth run of the session.

Functional images and statistical maps from different animals were registered into a common space by a two-step procedure. First, the brain-extracted global functional reference volume was registered to the brain-extracted structural volume. Second, the structural images of all animals were registered in a standardized space. The standardized space was created by co-registering and averaging structural volumes of four previously scanned macaque monkeys and aligning the resulting mean structural image along the anterior to posterior commissure line.

Brain voxels were determined from the high-resolution structural images using FSL's brain extraction tool (*bet*, Smith et al., 2004). Output of the brain extraction tool was corrected by hand in some difficult cases. These maps were registered to the low-resolution functional imaging space and served as masks for the detection of brain voxels (see below).

### 2.5. Functional connectivity

Functional connectivity was calculated for anatomically defined seed regions in several temporal waveband bands and with different amounts of spatial smoothing. The preprocessed time-series were demeaned and normalized by their standard deviation. Mean BOLD activity of all previously determined brain voxels was regressed out using FSL's linear regression tool (*fsl.glm*, Smith et al., 2004). These data were filtered with two Gaussian kernels with a standard deviation of 1 or 2 mm, respectively (*fslmaths*, Smith et al., 2004). The resulting 4D-volumes, including the original one without spatial smoothing, were filtered with a 400 s temporal high-pass (*fslmaths*, Smith et al., 2004) in order to remove low-frequency drift. In addition, we created a bandpassed version of the data by filtering with a 20 s low-pass. The preprocessing gave rise to 3 (spatial filters)  $\times$  2 (temporal filters)  $\times$  2 (cyclic artifact removal) = 12 4D-volumes for each original run.

To calculate functional connectivity of a seed region to the rest of the brain we averaged activity in this region and correlated it separately to the activity of all brain voxels. This procedure was repeated for all runs of the animal in question. For each voxel this rendered a set of six to eight correlation values, depending on the number of functional runs acquired for this animal. These values were transformed using Fischer's *z*-transformation and fed into a one-sample *t*-test. The resulting *t*-maps were corrected for multiple comparisons using a two-sided cluster criterion with a *t*-value cutoff of 2.3 and a critical cluster value of 0.05 (*cluster*, Smith et al., 2004).

## 3. Results

### 3.1. Heart and breathing rate

Before describing the cardiac and respiratory artifacts in detail we briefly report the properties of the cardiac and respiratory signals. For all monkeys, the average cardiac cycle was around 550 ms, slightly larger than a quarter of the TR. (monkey C:  $565\text{ ms} \pm 7$ ; monkey L:  $537\text{ ms} \pm 3$ ; monkey P:  $598\text{ ms} \pm 12$ ). An average respiratory cycle was around 2 s, on the order of magnitude of the TR (monkey C:  $1935\text{ ms} \pm 75$ ; monkey L:  $2025\text{ ms} \pm 67$ ; monkey P:  $2675\text{ ms} \pm 88$ ). In addition, we analyzed the variability of heart and breathing rate over the course of an individual run. For individual runs, the range of cardiac cycle durations, i.e., the longest cycle minus the shortest cycle, was 32 ms (monkey C:  $32\text{ ms} \pm 3$ ; monkey L:  $34\text{ ms} \pm 10$ ; monkey P:  $31\text{ ms} \pm 4$ ). The range of respiratory cycle durations, i.e., the duration of the longest cycle minus the duration of the shortest cycle, was 344 ms on average (monkey C:  $241\text{ ms} \pm 107$ ; monkey L:  $360\text{ ms} \pm 155$ ; monkey P:  $432\text{ ms} \pm 35$ ).

### 3.2. Cardiac artifacts

For all three monkeys a large number of voxels had significant cardiac artifacts (see Figs. 1a and 2a). Supplementary Fig. S1 shows

the cardiac artifact for an example voxel in the anterior cingulate. The bulk of voxels with cardiac artifacts was found close to the major arteries, such as the basilar artery and Circle of Willis, as well as the anterior, middle, and posterior cerebral arteries. Voxels around major veins seemed to be less affected. However, voxels around the superior sagittal sinus did show significant cardiac artifacts.

The most affected brain regions are (1) the ventral base of the cerebrum including the frontal pole of the temporal lobe, hypothalamus, parahippocampal cortex, and the entire brain stem, (2) the entire medial wall of the two hemispheres including anterior and posterior cingulate, and (3) regions in the fold of the sylvian fissure including the insula and auditory cortex (see Figs. 1a and 2c). This is likely to be due to the proximity of these regions to major vessels. Note that apart from the fourth ventricle, the other ventricles are not affected by the cardiac artifact.

### 3.3. Respiratory artifacts

For all three monkeys a large number of voxels had significant respiratory artifacts (see Figs. 1b and 2b). Supplementary Fig. S2 shows the respiratory artifact for an example voxel in the fourth ventricle. Voxels with significant respiratory artifacts were more common than voxels with significant cardiac artifacts. Part of the respiratory artifacts seemed to arise from breathing-related motion as opposed to breathing-related changes in blood oxygenation. To test this hypothesis we performed FSL's motion correction (*mcflirt*, Jenkinson et al., 2002) on the estimated artifact. For all three monkeys we found small but highly consistent breathing-related motion in the anterior–posterior and, with smaller amplitude, the ventro–dorsal direction. A study by Raj et al. (2001) concludes that analogous effects in humans are apparent motion caused by changes in bulk susceptibility in the lungs.

### 3.4. Spectral analysis of cardiac and respiratory artifacts

To determine the temporal properties of the artifacts we compared power spectra of the uncorrected and corrected data sets. We selected voxels with significant artifacts and calculated the mean power spectra of these voxels for the uncorrected and the corrected time-series. Fig. 3 shows the fraction of the corrected and uncorrected power spectra which corresponds to 1 minus the percent variance explained for the temporal waveband in question.

Cardiac artifacts were mainly found in wavelengths below 10 s (see Fig. 3a). In contrast, respiratory artifacts were observed also with longer wavelengths (see Fig. 3b). It is important to note that these differences are not an intrinsic property of the two signals, because the observed wavelength depends on the aliasing of the artifacts. The aliased frequency is determined by the difference between TR and the average duration and variability of the cardiac or respiratory cycle (e.g., Glover et al., 2000; Kiviniemi, Ruohonen, & Tervonen, 2005; Lund, 2001a). Aliasing into low frequency bands is especially likely to occur if the TR and duration of the artifactual cycle are similar. In line with this, we find an aliasing of the respiratory artifact into long wavelengths for monkeys C and L who have respiratory cycles of 1935 and 2025 ms, respectively, but not for monkey P with a respiratory cycle of 2675 ms (see Fig. 3b).

We simulated the effect of different TRs on the aliasing of the cardiac and respiratory artifacts. To do so, we used the estimated artifact  $a_c(\phi_c)$  of a strongly affected voxel, and determined the phase of the cardiac artifact  $\phi(n) = \phi_c(n \times TR)$  for a variety of different TRs. Then, we calculated the power spectra of the simulated artifacts  $a_c[\phi_c(n \times TR)]$  for all choices of TR. The results in Fig. 4a show that for a TR of 2 s (dotted line), the cardiac artifacts are aliased mainly into very short wavebands. In contrast, the respiratory artifacts are aliased to a wavelength of roughly 100 s. Furthermore,

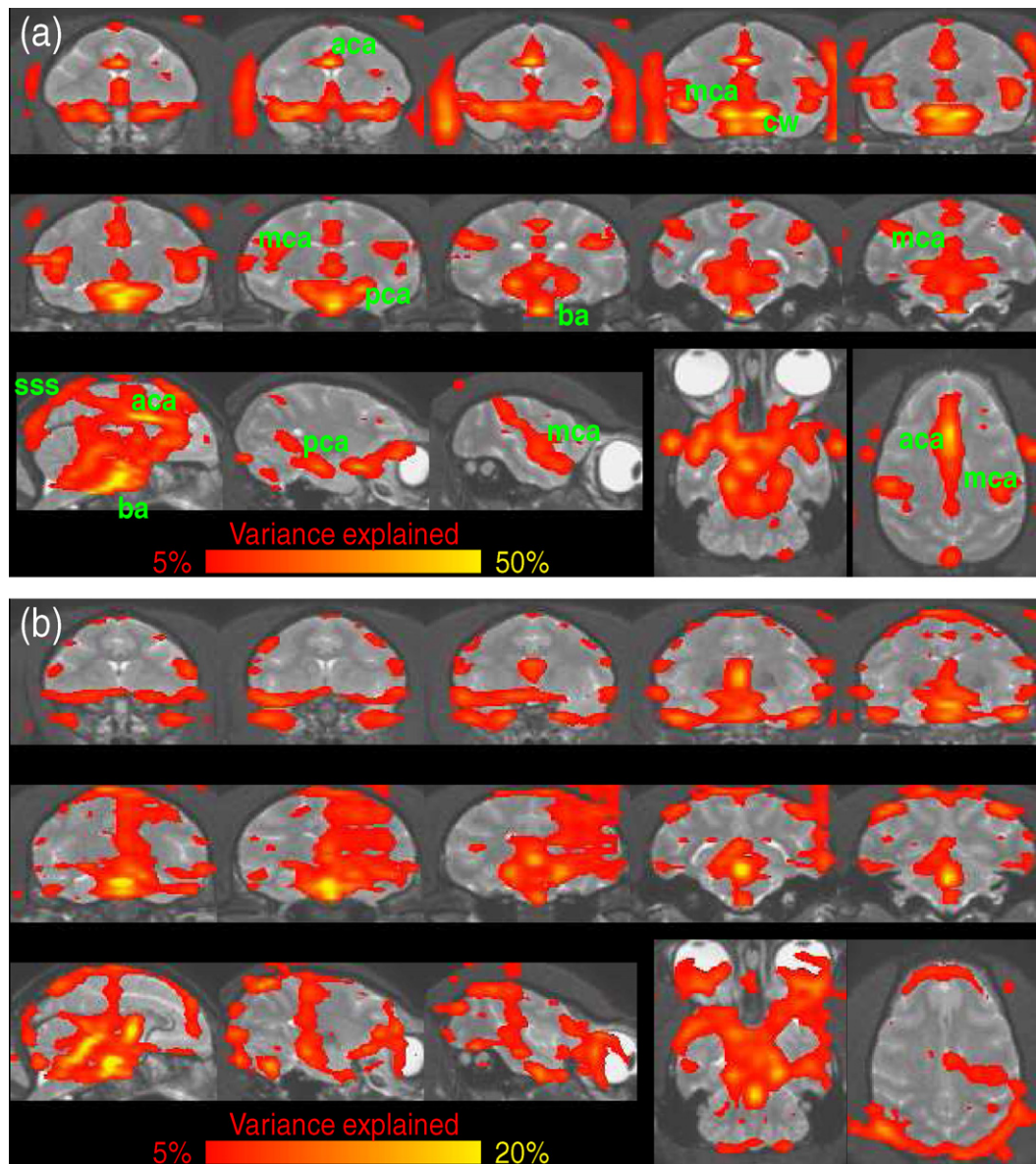


**Fig. 1.** Cardiac (a) and respiratory artifact (b) from one macaque monkey. Data were averaged over 8 runs of 400 volumes each. Regions with significant cyclic artifacts are overlaid on the individual T1-weighted structural image. The colors correspond to the percent variance explained by the harmonic regression. Note the different scales of the color bar for the cardiac and respiratory artifacts. (a) Regions with significant artifacts can be found around major vessels. The basilar artery (ba), anterior (aca), medial (mca) and posterior (pca) cerebral arteries can clearly be distinguished. Veins seem to cause less artifacts but the superior sagittal sinus (sss) is clearly visible. Arteries outside the brain such as the ophthalmic artery are also visible. (b) Part of the respiratory artifacts are caused by breathing-related apparent motion.

the simulation shows that for some choices of TR the cardiac artifacts can be expected in wavelengths well above 10 s. In such cases, low-pass filtering the data will not remove the cardiac artifacts.

### 3.5. Functional connectivity

The previous results have shown that a large fraction of voxels have significant cardiac and respiratory artifacts. In the following we will test how these artifacts affect functional connectivity maps. The impact of the cyclic artifacts was assessed by comparing results from three conditions. As a baseline we use the highpassed data set from which merely slow linear drifts had been removed. Results from this data set were compared to two artifact removal methods, the harmonic regression algorithm as well as the standard low-pass method.

### Example 1. Basilar artery seed

To test whether cyclic artifacts may affect fcMRI maps we selected a region which is highly affected by cyclic artifacts. The susceptibility maps suggest that the basilar artery can be considered such a worst case scenario. Selecting the basilar artery as a seed region has several advantages. First, under the assumption that there are no residual gray-matter voxels in the seed, we can assume that all observed correlations are not neuronally driven and hence artificial. Thus, to a first approximation, the improvement of the fcMRI maps can be quantified as the reduction in the number of voxels with a significant correlation. Second, in the event that we do find voxels with artificial correlations, it will serve as a benchmark test for the effectivity of the artifact removal method. If the method works, we would expect at least some of those correlations to disappear.

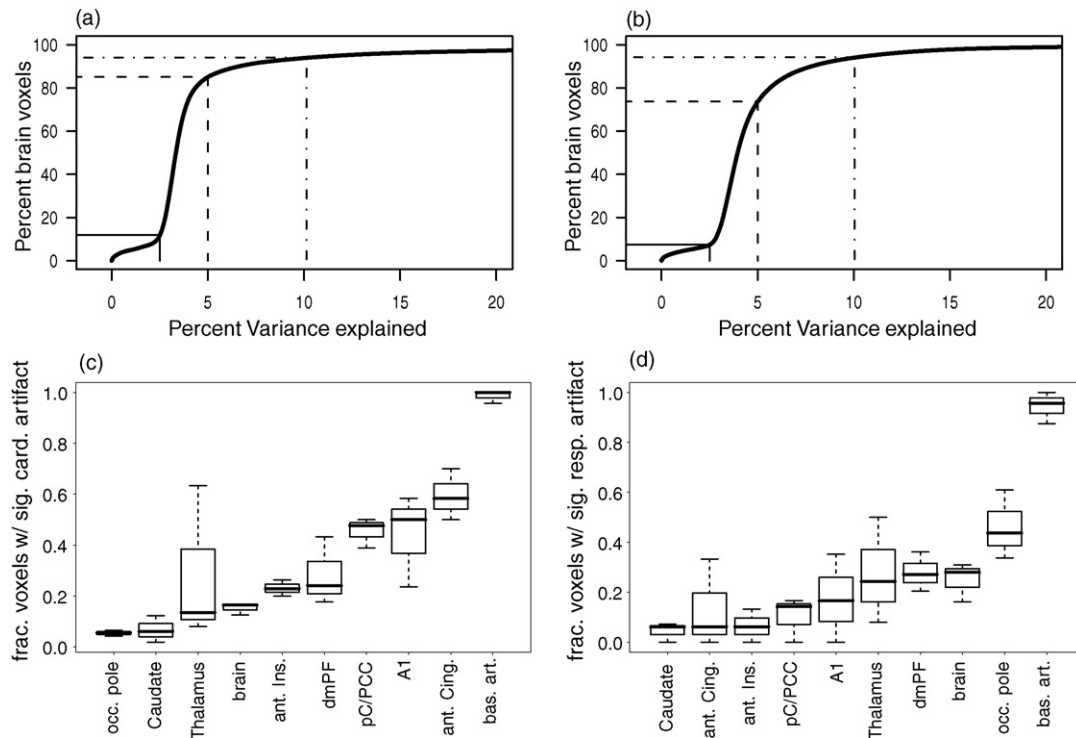


**Fig. 2.** Empirical distribution function of percent variance explained (a) by cardiac and (b) respiratory artifacts. All brain voxels of all three monkeys aggregated. The solid, dashed and dashed/dotted lines denote the values of the distribution function for 2.5, 5 and 10% variance explained. (c) Cardiac and (d) respiratory artifacts in different brain regions. Artifacts are quantified as the fraction of voxels with significant artifacts. occ. pole: occipital pole, aIC: anterior insular cortex, dmPF: dorso-medial prefrontal cortex, A1: primary auditory cortex, pC/PCC: posterior cingulate and posterior cuneal cortex (resting state seed), ant. Cing.: anterior cingulate, bas. art.: basilar artery, brain: all voxels assigned to neither of the specific regions.

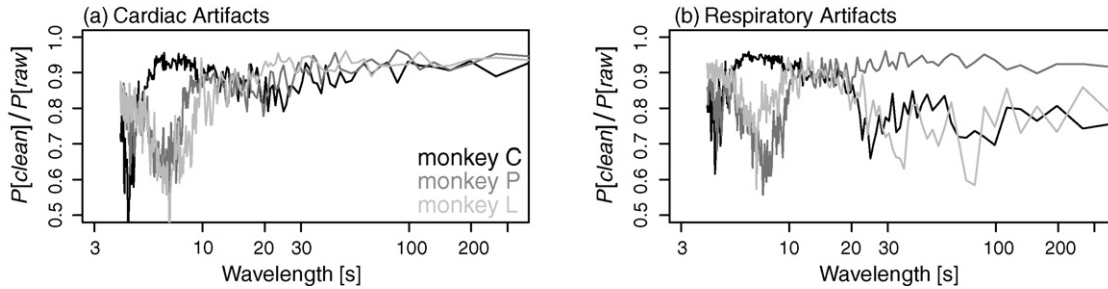


**Fig. 3.** Spectral analysis. Fraction of remaining power after removal of the cardiac (a) and respiratory artifacts (b). Different shades of gray correspond to the three different animals. Data are averaged over all runs and voxels with significant cardiac (a) and respiratory artifacts (b). Note that most of the artifacts are in the waveband below 10 s. However, some of the respiratory artifacts are in the waveband between 20 and 300 s. The differences between the animals are due to different cardiac and respiratory frequencies which cause an aliasing of the artifacts into different wavebands.

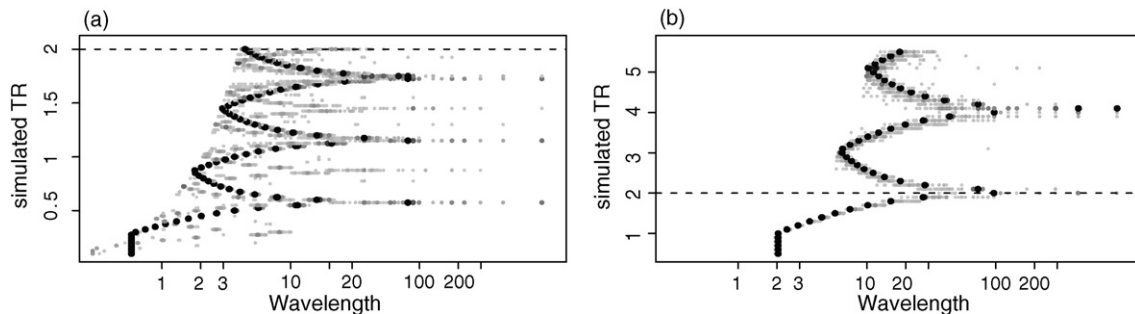


**Fig. 4.** Aliasing of (a) cardiac and (b) respiratory activity as a function of simulated TRs. Normalized luminance coded power spectra for cardiac and respiratory activity of a random run sampled at different simulated TRs. Large black dots denote wavelengths with maximal power, smaller gray dots denote wavelengths which are affected to a lesser degree. For TRs shorter than half the length of the average cycle (Nyquist frequency; 0.25 s for cardiac and 1 s for respiratory activity) the frequency analysis detects the power in the correct waveband. Longer TRs lead to an aliasing of the physiological activity into lower wavelengths. Note the large systematic change of the aliased wavelengths as a function of TR. For a TR of 2 s (dotted line) the predictions from the simulation match the data, i.e., cardiac artifacts are found mainly in a short wavelengths while respiratory artifacts are also found with longer wavelengths.

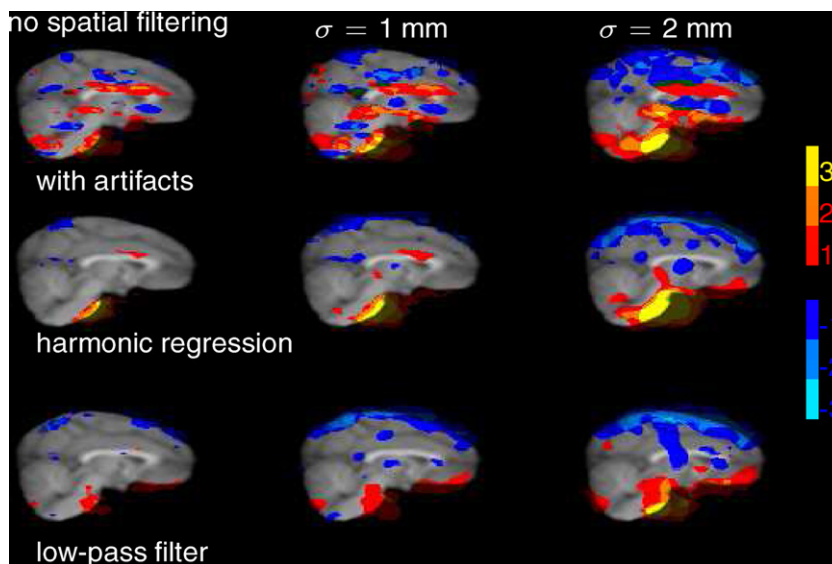


**Fig. 5.** Functional connectivity of the basilar artery seed. The different columns correspond to different amounts of spatial smoothing. The color code displays the number of animals with significant positive (red to yellow) and negative (dark to light blue) correlations to the seed region. A large fraction of the artificial correlations (top row) is removed by both the harmonic regression technique and the low-pass filter. It is important to note that the low-pass filter method works only if the cyclic artifacts are aliased into the corresponding waveband as happened to be the case here. The alternating horizontal stripes of positive and negative correlation are most likely due to differences in slice-time acquisition.

Fig. 5 shows the results of the fcMRI analysis for the basilar artery seed. For the data with the artifacts (top row) we find a large number of voxels with significant positive or negative correlations to the seed region. These artificial correlations are most pronounced for moderate spatial filtering, but can also be observed for no or strong spatial filtering. A closer inspection reveals a very prominent spatial pattern which consists of alternating stripes of positive and negative correlations. The orientation of the stripes is parallel to the slice orientation. We suggest that the pattern is due to differences in slice-time acquisition  $\delta_t$  which amount to an average phase shift  $\delta_\phi$  of the cardiac cycle between two voxels in different slices. Because the artifact as a function of phase is similar for most voxels  $a_1(\phi) \simeq a_2(\phi)$ , this shift determines the sign and magnitude of correlation  $\rho(a_1, a_2)$  between observed artifacts of two voxels in different slices,  $\rho(a_1, a_2) \simeq \rho(a_1(\phi), a_1(\phi + \delta_\phi))$ .

The bulk of these artificial correlations disappears after removing the cyclic artifacts (middle row, see Table 1 for details). This is a clear indication that (1) cyclic artifacts may affect fcMRI maps and (2) that the harmonic regression algorithm clearly reduces the impact of the artifacts. The alternating stripes of positive and negative correlations which can be observed in the data set with the artifacts disappear almost completely. These findings suggest that after removal of the artifacts the fcMRI maps reflect random spurious correlations as would be expected from any statistical method.

In the current case, the artifacts are removed just as effectively by standard low-pass filtering (third row). It is important to note that the low-pass filtering works if and only if the artifacts happen to be aliased into the high frequency range. While this happened to be the case for the cardiac artifacts in the present case (see Fig. 3), this is not the rule. As we show above, the cyclic artifacts may be aliased into any waveband (see Fig. 4). In such a case, the low-

pass method will be ineffective and render the same artificial fcMRI maps as the highpassed data (top row).

#### Example 2. Resting state network

A recent study has reported a network of correlated brain areas in anesthetized macaques (Vincent et al., 2007). The described network consisted of four regions which showed strong similarity to the so-called ‘resting state’ or ‘default’ network previously described for awake human subjects (Damoiseaux et al., 2006; Fox et al., 2005; Raichle et al., 2001): the posterior cingulate/precuneal cortex (pC/PCC), the dorsal medial prefrontal cortex (dmPFC), lateral temporo-parietal cortex (ITPC) and posterior parahippocampal cortex (pPHip). It is noteworthy that all of these regions are close to major vessels (pC/PCC and dmPFC are near the anterior cerebral artery; ITPC is near the middle cerebral artery; pPHip near the posterior cerebral artery, see also Fig. 6). Thus, the resting state network is optimally suited to test whether correlated cardiac artifacts can affect fcMRI of a realistic seed region, i.e., the pC/PCC.

Using moderate spatial filtering ( $\sigma = 1$  mm) we found correlations in brain areas which partially resemble the ones described by Vincent et al. (2007). Significant positive correlations were found mainly in the ITPC (see Fig. 6 top row). Significant positive correlations were less consistent in pPHip and completely absent in the dmPFC. Despite the differences, these results were sufficient to test whether the observed correlations in the ITPC were affected by cyclic artifacts. Indeed, after removal of the artifacts the number of voxels with positive correlations in ITPC and pPHip was clearly reduced (Fig. 6 middle row). This suggests that even for realistic seed regions like the pC/PCC, fcMRI maps may be affected by cyclic artifacts.

As for the basilar artery seed, we expected the low-pass method to be just as effective in the current case. However, the low-passed data revealed the same pattern of positive correlations in ITPC as the highpassed data (Fig. 6 bottom vs. top row). This seems to suggest that in this case the low-pass method was less effective at removing the cyclic artifacts. There is an alternative explanation for this finding: assume that there are two independent sources which give rise to the positive correlations in ITPC, one artificial source linked to the cyclic artifacts,

**Table 1**  
Percent voxels with significant positive and negative correlation to the basilar artery seed region in the condition with moderate spatial filtering ( $\sigma=1$ mm).

	Monkey L	Monkey P	Monkey C
With artifacts	6.3/7.7%	9.2/10.6%	5.3/6.3%
Without artifacts	1.7/1.9%	2.8/3.7%	3.9/5.5%
Low-passed	1.9/2.2%	13.2/14.2%	2.2/3.7%

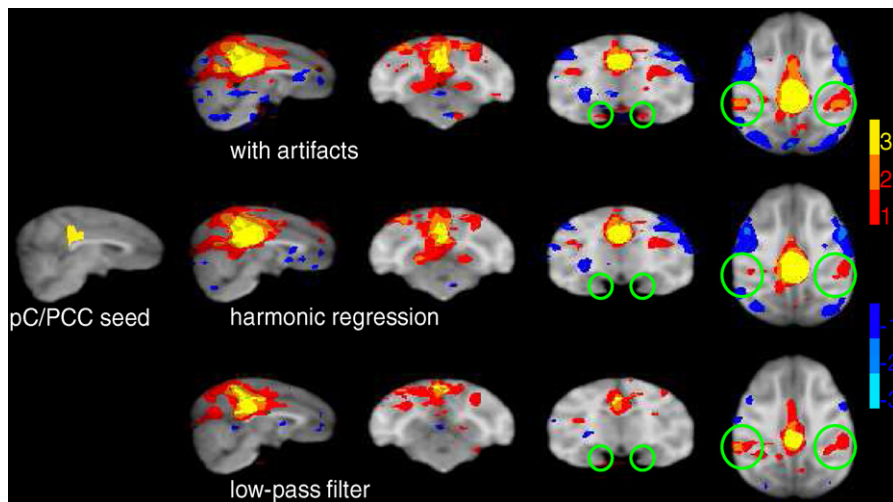


**Fig. 6.** ‘Resting state’ network. fMRI maps for a seed in the posterior cingulate/precuneal cortex (leftmost panel). Conventions as in Fig. 5. Regions with significant correlations were found in the lateral temporo-parietal cortex and posterior parahippocampal cortex (top row). In contrast to previous fMRI studies, no correlations were found in the dorso-medial prefrontal cortex. The number of voxels with significant correlations in the lateral temporo-parietal cortex and the posterior parahippocampal cortex was reduced by the harmonic regression method (middle row) and to a lesser degree by the low-pass filtering (bottom row).

and another source which probably reflects correlated neuronal activity. Removing the cyclic artifacts reduced the number of positive voxels by removing the artificial source of correlation. The residual correlations of neuronal origin were lost because of uncorrelated noise. The low-pass filter removed not only the cyclic artifacts (which happened to be aliased to this waveband) but also a big amount of the uncorrelated noise. Hence, by removing both correlated and uncorrelated artifacts the correlations of putatively neuronal origin are now able to reach significance.

#### 4. Discussion

Cardiac and respiratory artifacts were mapped in lightly anesthetized macaque monkeys. The artifacts were found to have a spatially and temporally non-uniform effect on BOLD signals. The spatial distribution of the artifacts was similar to that previously described for awake humans (Cordes et al., 2001; Glover et al., 2000; Harvey et al., 2008; Lund et al., 2006). The bulk of the cardiac artifacts were found close to major vessels. Respiratory artifacts were mainly found in regions with a high spatial derivative as found, for example, at the fringes of the brain, and could be explained by breathing-related (apparent) motion. Depending on the rate as well as the variability of the respiratory and cardiac cycle, the corresponding artifacts were aliased into a wide range of temporal wavebands (Biswal et al., 1996; Glover et al., 2000; Lund, 2001a; Lund et al., 2006). In cases where the artifacts are aliased to wavebands typically used for fMRI (~10/20–400 s), they will have a profound impact on fMRI maps if the seed region is affected by the artifacts. These findings complement studies showing that the removal of cyclic artifacts improves the quality of statistical inferences for standard fMRI GLM analyses (Harvey et al., 2008; Lund et al., 2006).

##### 4.1. Necessary, sufficient and modulating conditions

Our results show that under certain conditions the removal of the cyclic cardiac and respiratory artifacts may have a profound impact on fMRI. In the following we describe the factors that determine whether cyclic artifacts will cause artificial correlations.

**Spatial restrictions.** Two voxels may show artificial correlations only if both of them are affected by the artifact. Thus, if the seed

region itself is not affected then the entire fMRI map will not be affected. If the seed region is affected, there is a chance that other affected voxels may show artificial positive or negative correlations (see Fig. 5 and 6).

**Temporal restrictions.** Our results and our simulations show that cardiac and respiratory artifacts can be aliased into a variety of different wavebands (see Figs. 3 and 4; also refer to citations Biswal et al., 1996; Glover et al., 2000; Lund, 2001a; Lund et al., 2006). The aliased wavelength is determined by the TR and the cardiac/respiratory frequency. The artifacts will affect fMRI only if they are aliased into the waveband used for fMRI. Typical choices of TR and values of cardiac/respiratory frequency can easily lead to an aliasing into wavelengths from 10/20 to 400 s which are typically used for fMRI. Thus, adequate temporal filtering may reduce the effects of artifacts in some cases, but it is not a reliable substitute for more sophisticated artifact removal algorithms.

**Spatial smoothing.** Due to differences in slice-time acquisition, the artifacts in different slices of a volume are sampled during different phases of the artifact. Such differences in acquisition time may introduce high spatial frequencies in the direction perpendicular to the slices. The presence of high spatial frequencies is determined by the mean difference in the phase of the artifacts for adjacent slices. If the difference is large, i.e., close to  $\pi$ , the artifacts will have high spatial frequency content perpendicular to the slices. In such a case any kind of spatial smoothing will attenuate the artifacts. Spatial smoothing may occur explicitly as part of the standard preprocessing routine or implicitly during motion correction and registration. Another source of spatial smoothing comes from the averaging of activity of all voxels in the seed region. Thus, if the seed region spans several slices, averaging the activity may cancel out a considerable fraction of the artifact. However, even with explicit spatial smoothing, motion correction and a seed region spanning several slices, cardiac and respiratory artifacts still had a significant effect on our fMRI maps (see Fig. 5 and 6). Thus, spatial smoothing may reduce the effects of the artifacts sometimes, but they are no substitute for an actual artifact removal algorithm.

**Slice acquisition time and slice orientation.** If spatial and temporal restrictions for the presence of artifacts are met, fMRI maps will be affected by the artifacts. The precise pattern of artificial correlations is determined by seemingly unrelated parameters such as slice-timing and slice orientation. The average difference in slice

acquisition time between voxels in the seed region and the voxel in question will determine the sign and magnitude of the artificial correlations. The slice orientation will determine the difference in slice acquisition time between a voxel and the average voxel in the seed region. Taken together the two parameters determine the spatial pattern of the artificial correlation in affected brain regions (see top row in Fig. 5)

#### 4.2. Resting state network

We investigated the effects of cyclic artifacts on fcMRI of the PC/PCC, a well-studied brain region which has been implicated to play an important role in the so-called resting state network. We found significant positive correlations in the ITPC as previously described for anesthetized macaque monkeys (Vincent et al., 2007). However, correlations in the pPHip and dmPFC were less reliable or completely absent. Comparing the results before and after removal of the artifacts we conclude that correlations in the ITPC and the pPHip may be overestimated if cyclic artifacts are not removed. However, our results are in line with the assumption that a significant part of the correlations between PC/PCC and ITPC were not caused by cyclic artifacts. This is in line with a previous study which showed that the correlations in the resting state network are not due to changes in blood oxygenation caused by slow fluctuations in breathing rate or depth (Birn, Diamond, Smith, & Bandettini, 2006). In summary, our findings clearly outline the necessity to include sophisticated artifact removal algorithms such as RETROICOR into the standard fcMRI preprocessing pipeline even when using realistic seed regions which are only moderately affected by cyclic artifacts.

#### 4.3. Comparison of artifact removal methods

Our data show that, as predicted by Lund (2001a), standard low-pass filtering does not adequately remove artificial correlations from fcMRI data. In the present paper we used harmonic regression to remove the cyclic cardiac and respiratory artifacts. A number of alternative methods with different advantages and requirements have been suggested in the literature (e.g., Biswal et al., 1996; Frank, Buxton, & Wong, 2001; Glover et al., 2000; Hu et al., 1995; Josephs, Howseman, Friston, & Turner, 2001; Lund, 2001b; Lund et al., 2006; Mitra et al., 1997; Thomas, Harshman, & Menon, 2002). A review of most of these methods is provided in Lund et al. (2006). It was beyond the scope of our study to systematically compare the effectiveness of these methods. All of these methods have been shown to remove significant fractions of the artifacts. Our results suggest that either one of them will help reduce the number of false positive correlations.

### 5. Conclusions

Our results show that standard preprocessing steps which include spatial and temporal low-pass filtering are not sufficient to exclude artificial correlations in studies of functional connectivity, unless the TR is short enough to prevent aliasing. The precise spatial pattern of artificial correlations depends on the interaction of a number of factors such as TR, cardiac frequency, respiratory frequency, slice-timing and slice orientation. These intricate interactions may give rise to spatial patterns of artificial correlations which are hard to distinguish from patterns of neuronally driven correlations.

### Acknowledgments

We want to thank Girma Asfaw and Stephen Dashnaw for their help with animal preparation and data acquisition. Thanks to Yev-

geniy Sirotnin, Aniruddha Das, Franco Pestilli and Marianna Yanike for helpful discussions. We also want to acknowledge the support of Daniel Salzman and Jacqueline Gottlieb who let us scan their monkeys. Funded by NIH-MH073821.

### Appendix A. Supplementary Data

Supplementary data associated with this article can be found, in the online version, at doi:10.1016/j.neuropsychologia.2009.11.026.

### References

- Auer, D. P. (2008). Spontaneous low-frequency blood oxygenation level-dependent fluctuations and functional connectivity analysis of the 'resting' brain. *Magnetic Resonance Imaging*, 26(7), 1055–1064.
- Birn, R. M., Diamond, J. B., Smith, M. A., & Bandettini, P. A. (2006). Separating respiratory-variation-related fluctuations from neuronal-activity-related fluctuations in fMRI. *Neuroimage*, 31(4), 1536–1548.
- Biswal, B., DeYoe, A. E., & Hyde, J. S. (1996). Reduction of physiological fluctuations in fMRI using digital filters. *Magnetic Resonance in Medicine*, 35(1), 107–113.
- Brewer, A. A., Press, W. A., Logothetis, N. K., & Wandell, B. A. (2002). Visual areas in macaque cortex measured using functional magnetic resonance imaging. *Journal of Neuroscience*, 22(23), 10416–10426.
- Cordees, D., Houghton, V. M., Arfanakis, K., Carew, J. D., Turski, P. A., Moritz, C. H., et al. (2001). Frequencies contributing to functional connectivity in the cerebral cortex in "resting-state" data. *American Journal of Neuroradiology*, 22(7), 1326–1333.
- Dagli, M. S., Ingeholm, J. E., & Haxby, J. V. (1999). Localization of cardiac-induced signal change in fMRI. *Neuroimage*, 9(4), 407–415.
- Damoiseaux, J. S., Rombouts, S. A. R. B., Barkhof, F., Scheltens, P., Stam, C. J., Smith, S. M., et al. (2006). Consistent resting-state networks across healthy subjects. In *Proceedings of the National Academy of Sciences USA*, 103(37) (pp. 13848–13853).
- Essen, D. C. V., Lewis, J. W., Drury, H. A., Hadjikhani, N., Tootell, R. B., Bakircioglu, M., et al. (2001). Mapping visual cortex in monkeys and humans using surface-based atlases. *Vision Research*, 41(10–11), 1359–1378.
- Fox, M. D., Snyder, A. Z., Vincent, J. L., Corbetta, M., Essen, D. C. V., & Raichle, M. E. (2005). The human brain is intrinsically organized into dynamic, anticorrelated functional networks. In *Proceedings of the National Academy of Sciences USA*, 102(27) (pp. 9673–9678).
- Frank, L. R., Buxton, R. B., & Wong, E. C. (2001). Estimation of respiration-induced noise fluctuations from undersampled multislice fMRI data. *Magnetic Resonance in Medicine*, 45(4), 635–644.
- Glover, G. H., & Lee, A. T. (1995). Motion artifacts in fMRI: Comparison of 2dft with pr and spiral scan methods. *Magnetic Resonance in Medicine*, 33(5), 624–635.
- Glover, G. H., Li, T. Q., & Reiss, D. (2000). Image-based method for retrospective correction of physiological motion effects in fMRI: Retroicor. *Magnetic Resonance in Medicine*, 44(1), 162–167.
- Hadj-Bouziane, F., Bell, A. H., Knutsen, T. A., Ungerleider, L. G., & Tootell, R. B. H. (2008). Perception of emotional expressions is independent of face selectivity in monkey inferior temporal cortex. *Proceedings of the National Academy of Sciences USA*, 105(14), 5591–5596.
- Harvey, A. K., Pattinson, K. T. S., Brooks, J. C. W., Mayhew, S. D., Jenkinson, M., & Wise, R. G. (2008). Brainstem functional magnetic resonance imaging: Disentangling signal from physiological noise. *Journal of Magnetic Resonance Imaging*, 28(6), 1337–1344.
- Hu, X., Le, T. H., Parrish, T., & Erhard, P. (1995). Retrospective estimation and correction of physiological fluctuation in functional MRI. *Magnetic Resonance in Medicine*, 34(2), 201–212.
- Jenkinson, M., Bannister, P., Brady, M., & Smith, S. (2002). Improved optimization for the robust and accurate linear registration and motion correction of brain images. *Neuroimage*, 17(2), 825–841.
- Josephs, O., Howseman, A., Friston, K., & Turner, R. (2001). Physiological noise modelling for multi-slice epifMRI using spm. In *Proceedings of the 5th annual meeting of ISMRM*
- Kiviniemi, V., Ruohonen, J., & Tervonen, O. (2005). Separation of physiological very low frequency fluctuation from aliasing by switched sampling interval fMRI scans. *Magnetic Resonance Imaging*, 23(1), 41–46.
- Logothetis, N. K., Guggenberger, H., Peled, S., & Pauls, J. (1999). Functional imaging of the monkey brain. *Nature Neuroscience*, 2(6), 555–562.
- Lowe, M. J., Mock, B. J., & Sorenson, J. A. (1998). Functional connectivity in single and multislice echoplanar imaging using resting-state fluctuations. *Neuroimage*, 7(2), 119–132.
- Lund, T. E. (2001a). fcMRI—mapping functional connectivity or correlating cardiac-induced noise? *Magnetic Resonance in Medicine*, 46(3), 628–629.
- Lund, T. E. (2001b). fMRI using vessel time-series as covariates in a general linear model. In *Proceedings of the 9th annual meeting of ISMRM*.
- Lund, T. E., Madsen, K. H., Sidaros, K., Luo, W.-L., & Nichols, T. E. (2006). Non-white noise in fMRI: Does modelling have an impact? *Neuroimage*, 29(1), 54–66.
- Maldjian, J. A. (2001). Functional connectivity MR imaging: Fact or artifact? *American Journal of Neuroradiology*, 22(2), 239–240.
- Mardia, K. (1972). *The statistics of directional data*. New York: Academic Press.

- Mitra, P. P., Ogawa, S., Hu, X., & Ugurbil, K. (1997). The nature of spatiotemporal changes in cerebral hemodynamics as manifested in functional magnetic resonance imaging. *Magnetic Resonance in Medicine*, 37(4), 511–518.
- Pinsk, M. A., DeSimone, K., Moore, T., Gross, C. G., & Kastner, S. (2005). Representations of faces and body parts in macaque temporal cortex: A functional MRI study. *Proceedings of the National Academy of Sciences USA*, 102(19), 6996–7001.
- Raichle, M. E., MacLeod, A. M., Snyder, A. Z., Powers, W. J., Gusnard, D. A., & Shulman, G. L. (2001). A default mode of brain function. *Proceedings of the National Academy of Sciences USA*, 98(2), 676–682.
- Raj, D., Anderson, A. W., & Gore, J. C. (2001). Respiratory effects in human functional magnetic resonance imaging due to bulk susceptibility changes. *Physics in Medicine and Biology*, 46(12), 3331–3340.
- Rogers, B. P., Morgan, V. L., Newton, A. T., & Gore, J. C. (2007). Assessing functional connectivity in the human brain by fMRI. *Magnetic Resonance Imaging*, 25(10), 1347–1357.
- Smith, S. M., Jenkinson, M., Woolrich, M. W., Beckmann, C. F., Behrens, T. E. J., Johansen-Berg, H., et al. (2004). Advances in functional and structural MR image analysis and implementation as FSL. *Neuroimage*, 23(Suppl. 1), 208–S219.
- Thomas, C. G., Harshman, R. A., & Menon, R. S. (2002). Noise reduction in bold-based fMRI using component analysis. *Neuroimage*, 17(3), 1521–1537.
- Tsao, D. Y., Freiwald, W. A., Knutsen, T. A., Mandeville, J. B., & Tootell, R. B. H. (2003). Faces and objects in macaque cerebral cortex. *Nature Neuroscience*, 6(9), 989–995.
- Vincent, J. L., Patel, G. H., Fox, M. D., Snyder, A. Z., Baker, J. T., Essen, D. C. V., et al. (2007). Intrinsic functional architecture in the anaesthetized monkey brain. *Nature*, 447(7140), 83–86.